Journal of Molecular Liquids 315 (2020) 113769

Contents lists available at ScienceDirect

Journal of Molecular Liquids

journal homepage: www.elsevier.com/locate/molliq

Graphene oxide-manganese ferrite ($GO\text{-}MnFe_2O_4$) nanocomposite: One-pot hydrothermal synthesis and its use for adsorptive removal of Pb^{2+} ions from aqueous medium

Monu Verma [a,*], Ashwani Kumar [b], Krishna Pal Singh [c], Ravi Kumar [d], Vinod Kumar [e], Chandra Mohan Srivastava [f], Varun Rawat [f], Gyandeshwar Rao [f], Sujata Kumari [f], Pratibha Sharma [f], Hyunook Kim [a,*]

[a] Department of Environmental Engineering, University of Seoul, Seoul 130743, South Korea
[b] Institute Instrumentation Centre, Indian Institute of Technology Roorkee, Roorkee 247667, India
[c] DAV(PG) College muzaffarnager, 251001, Uttar Pradesh, India
[d] Department of Chemistry, National Institute of Technology Srinagar, Jammu & Kashmir 190006, India
[e] Department of Chemistry, Uttaranchal University, Dehradun 248007, India
[f] Department of Chemistry, Amity School of Applied Sciences, Amity University Haryana, Gurugram 122413, India

ARTICLE INFO

Article history:
Received 19 April 2020
Received in revised form 21 June 2020
Accepted 6 July 2020
Available online 7 July 2020

Keywords:
Nanocomposite
Heavy metals
Adsorption kinetics
Isotherm
Water treatment

ABSTRACT

Herein, we showed that the graphene oxide with manganese ferrite ($GO\text{-}MnFe_2O_4$) possess great adsorption properties for the selective Pb^{2+} ions removal from the aqueous medium. Nanocomposite adsorbent was developed by one-pot hydrothermal method, using graphene oxide as a supporting material to minimize the aggregation of $MnFe_2O4$. Also, GO possesses important role in the adsorption mechanism of Pb^{2+} through electrostatic/ionic interactions. The characterizations such as FT-IR, XPS, P-XRD, FE-SEM, and BET of the synthesized nanocomposite were carried out to assess the different properties such as functionalities, crystallinity, morphology, and surface area value, respectively. Thereafter, the adsorption performance of $GO\text{-}MnFe_2O_4$ nanocomposite was tested for the Pb^{2+} at various adsorption parameters including to contact time, solution pH, adsorbent dose, and concentration of initial Pb^{2+} in order to measure the optimum adsorption condition. Kinetic experiments suggest that the equilibrium attained in 30 min and followed a pseudo-second-order kinetic model. Adsorption isotherm model followed to Langmuir isotherms and gives a maximum adsorption capacity of 621.11 mg/g. The reusability tests exhibited good durability and good efficiency for repeated Pb^{2+} adsorptions with $GO\text{-}MnFe_2O_4$ nanocomposite. These results demonstrated that the $GO\text{-}MnFe_2O_4$ nanocomposite may be an attractive adsorbent having low-cost for the effectively Pb^{+2} removal of from the polluted water.

1. Introduction

In the recent decades, the environmental pollution accompanied by growing global industrialization and agricultural/domestic activities such as the presence of heavy metals (e.g., arsenic, cadmium, mercury, lead, chromium, selenium etc.) in aquifer systems exerted potential negative effects on human health and ecological systems. Among various heavy metal ions, lead (Pb^{2+}) is a non-biodegradable, highly toxic and wide spread contaminant in aqueous solutions which has the ability to produce disorders related with genotoxic, neurological carcinogenic, and reproductive defects in the human [1]. It is among top 20 hazardous pollutants which has been identified by United States Environmental Protection Agency (USEPA) and Agency for Toxic Substances and Disease Registry (ATSDR) [2]. The maximum acceptance limit of Pb^{2+} is 0.05 mg/L and 0.015 mg/L according to Bureau of Indian Standards (BIS) and World Health Organization (WHO), respectively, in potable water [3]. Therefore, effectively Pb^{2+} removal from aqueous solutions is a challenging task for the scientific community to prevent the adverse effects on the human health and environment.

A number of different technologies such as chemical oxidation/reduction [4] membrane separation [5], electrochemical treatment [6], coagulation/flocculation [7], chemical precipitation [8], ion exchange [9], and adsorption [10,11] have been successfully applied for the Pb^{2+} removal from aqueous medium. Among them, the adsorption is one of the effective technique for this purpose as it is cost effective, simple and rapid, produce minimum sludge, highly efficient and reproducible [12,13].

Literature survey revealed the use of different type of materials including activated carbons [14], polymers [15], and nanomaterial based

* Corresponding authors.
E-mail addresses: mkvcyiitr@gmail.com (M. Verma), h_kim@uos.ac.kr (H. Kim).

https://doi.org/10.1016/j.molliq.2020.113769
0167-7322/

adsorbent for example carbon nanotubes, graphene, metal oxides/magnetic nanoparticles and their composite/hybrid [16–18] for the pollutants removal from the aqueous medium. Among them, activated carbon is most widespread and accepted materials for wastewater treatment among the different adsorbents. This is due to having porous structure which resulted in high surface area for pollutants removal. However it is restricted due to energy intensiveness as 500–900 °C required for the regeneration and it also have limited removal efficiency for many hydrophilic micropollutants [19]. Different types of spinel ferrites (MFe_2O_4 where M = Fe^{2+}, Mn^{2+}, Ni^{2+}, Co^{2+}etc.) nanocomposite have been reported for the effectively heavy metal ions removal [20]. The efficiency of such spinel nanocomposites are limited for heavy metal ions removal from aqueous solutions due to their aggregation tendency which does not allowed them for practical applications [21,22]. Hence, the modification in spinel nanocomposites is required for the acceptable heavy metal ions removal with fast adsorption rate. Recently, a single layer carbon sheet of graphene having a hexagonal packed lattice structure showed interesting physio-chemical properties because of large theoretical specific surface area value (2630 m^2/g) [23]. Graphene oxide (GO), a oxidise form of graphene based material has been reported to have large number of oxygenated functionalities, non-toxic nature and low cost which makes them an impressive modifier for the heavy metals removal [24,25]. Some researchers have reported the removal of different heavy metals such as As^{3+}, As^{5+}, Cd^{2+}, Pb^{2+} and rare earth elements (La^{3+} and Ce^{3+}) using GO-$MnFe_2O_4$ nanocomposite from the contaminated water. For example, Kumar et al. reported the hybrid single-layer graphene oxide with magnetic $MnFe_2O_4$ nanoparticles synthesized via the coprecipitation technique for the adsorptive removal of As^{3+} and As^{5+} from the contaminated water with maximum adsorption capacity 146 and 207 mg/g, respectively [26]. Chella et al. reported the solvothermal synthesis of $MnFe_2O_4$-graphene composite for the Pb^{2+} and Cd^{2+} removal with adsorption capacity of 100 mg/g and 76.90 mg/g, respectively at pH 5 and 7 [27]. Peng et al. reported the synthesis of graphene oxide/$MnFe_2O_4$ motor via green route and found 100 mg/g adsorption capacity for both Pb^{2+} and Cd^{2+} heavy metals for the removal of Pb^{2+} and Cd^{2+} heavy metals [28]. Xu et al. were reported the synthesis of GO/$MnFe_2O_4$ via hydrothermal process and found the adsorption capacity 133.3 mg/g for Pb^{2+} through Langmuir isotherm model [29]. Ghobadi and co-workers reported the removal of La^{3+} and Ce^{3+} at room temperature using $MnFe_2O_4$-GO with 1001 and 982 mg/g adsorption capacity, respectively [30]. However, synthesis of GO-$MnFe_2O_4$ via one-pot hydrothermal nanocomposite and it's use for selective Pb^{2+} removal from aqueous solution have never been reported to the best of our knowledge. Therefore, we reported here the synthesis of GO-$MnFe_2O_4$ nanocomposite via one-pot hydrothermal process for Pb^{2+} removal. It also includes the investigation on its adsorption efficiency for the Pb^{2+} ions removal in relation to adsorption related parameters.

2. Experimental and methods

2.1. Materials

All the chemicals were used of analytical grade: natural graphite powder (200 mesh), concentrated sulfuric acid (H_2SO_4, 98%) and ethanol (C_2H_5OH), sodium nitrate ($NaNO_3$), hydrogen peroxide (H2O2, 30%), permanganate ($KMnO_4$, 99.9%), ferrous sulfate hexahydrate ($FeCl_3 \cdot 6H2O$, ≥99%), manganese (II) sulfate tetrahydrate ($MnCl2 \cdot 4H2O$, ≥99%), hydrogen chloride (HCl, 37%), sodium hydroxide (NaOH, 99%) and lead nitrate ($PbNO_3$) were procured from Merck India Ltd., Mumbai, India.

2.2. Synthesis of GO

Modified Hummer's method was used for the preparation of GO from the graphite powder [31]. In this process, 1.2 g graphite powder and 2.0 g sodium nitrate were added in 50 mL concentrated H_2SO_4 followed by continuous stirring for 2 h in a salt bath between 0 °C–6 °C temperature. Subsequently, 6.0 g $KMnO_4$ was added slowly to this reaction mixture while maintaining the same temperature. Stirring was continuing for an additional 2.0 h then increase the temperature of reaction mixture up to 40 °C. Then, 100 mL distilled water (DI) was added and the temperature of the mixture was raised to 100 °C and stirred for additional half an hour. With 150 mL DI water, the mixture was again diluted and 8 mL H_2O_2 was added drop wise to the mixture. The appearance of yellow color confirms the formation of GO. The suspended mixture was centrifuged and then washed with 8% hydrogen chloride and DI water to make the solution neutralize. Finally, the centrifuged solid material was dried at 50 °C to obtain GO powder.

2.3. Synthesis of GO-$MnFe_2O_4$ nanocomposite

GO-$MnFe_2O_4$ nanocomposite was synthesized using one-pot hydrothermal process. In a typical synthesis, 0.5 g GO was firstly dispersed in 100 mL DI water and sonicated it for 1 h. 3.24 g $FeCl_3 \cdot 6H_2O$ and 0.94 g $MnCl_2 \cdot 4H_2O$ were added in the sonicated GO and it was additionally stirred it for 1 h. 50 mL NaOH (pH = 11) was added with continue stirring and reaction mixture was stirred for additional 20 min. After that, the homogeneous mixture was sealed into a Teflon-lined stainless autoclave, and heated at 140 °C for 12 h. Then it was removed from the oven and cooled to room temperature. The precipitated GO-$MnFe_2O_4$ sample was filtered from the solution. It was washed thoroughly with DI water, and dried in the vacuum oven at 50 °C for over 12 h.

2.4. Characterization

The phase purity and crystalline nature was analyzed on Powder X-ray diffraction (P-XRD), Bruker D8 Advance X-ray diffractometer with monochromatic Cu K_α ($\lambda = 1.5418$ Å) radiation at a scan rate (2θ) of 2° per min, an accelerated voltage (40 kV) and the applied current (30 mA) in the range of 5° to 80°. X-ray photoelectron spectroscopy (XPS) was performed on PHI Versa Probe III, using Al K_α radiation source (1486.708 keV, step width = 0.05 eV, pass energy = 55 eV, base pressure of 10–7 mbar). Fourier transform infrared (FT-IR) spectrum was recorded in the form of KBr pellet in the range of 400–4000 cm^{-1} on a Nicolet NEXUS Aligent 1100 spectrophotometer. The morphology of sample was examined with Zeiss, Ultra plus 55 Field emission scanning electron microscopy (FES-EM). Energy dispersive X-ray (EDX) analysis attached with FE-SEM was used for the elemental analysis of the samples. The surface area value and pore size distribution measurements were performed using Brunauer, Emmet, and Teller (BET), and Barrett, Joyner, Halenda (BJH) methods, respectively on Autosorb-1-C, Quantachrome, USA at 77 K. The materials were degassed for 8 h at 150 °C prior to the N_2 adsorption/desorption measurements. Atomic adsorption spectroscopy (AAS), AAnalyst 800, Perkin Elmer Company, USA was used to quantitatively measure the Pb^{2+} ions concentration.

2.5. Batch adsorption experiment

All the batch adsorption experiments were carried out at room temperature using standard stock solution for the adsorptive removal of Pb^{2+}. The stock solution was prepared by dissolving 1.598 g lead nitrate in one litre DI water. The desired concentration of the required solutions was obtained by dilution method. The optimum conditions for Pb^{2+}adsorption by GO-$MnFe_2O_4$ nanocomposite was investigated using a mixture of specific amount of material, 8 mg/50 mL working solution of Pb^{2+} in a 100 mL Erlenmeyer flask as reported earlier by our research group [32]. The investigation of pH effect was carried out in the pH range 1–6 by using 50 mL of 50 mg/L lead solution. The adjustment in the pH of the solution was carried out by 1.0 M HNO_3 and 1.0 M NaOH according to requirement. Dose effect of the synthesized GO-$MnFe_2O_4$ nanocomposite adsorbent was investigated in the range of 2–30 mg per 50 mL of 50

mg/L Pb^{2+} concentration. Contact time was used in the range of 5–120 min with the 50 mg/L concentration of Pb^{2+} ions and dosage 8 mg corresponding to the pH at which maximum adsorption occur. In order to determine the adsorption equilibrium isotherm, the different concentrations have been used in the range of 10–300 mg/L of Pb^{2+} solutions. During all the experiments, the flasks were shaken at 300 rotations per minutes (rpm) in a water bath shaker. After completing the adsorption process, the supernatant was separated by centrifuge and magnet from the mixture in order to analyze the remaining Pb^{2+}concentrations using AAS. The removal efficiencies and adsorption capacity (q_e) of the synthesized adsorbent were find out by using the equations given below:

$$\text{Removal efficiency } (\%) = \left(\frac{C_0 - C_e}{C_0}\right) \times 100 \quad (1)$$

$$\text{Adsorption capacity } (q_e) = (C_0 - C_e)\frac{V}{M} \quad (2)$$

where, C_o and C_e represent the concentrations of Pb^{2+} ions initially and at equilibrium stage respectively, while m (g) and V (L) signify the weight of the adsorbent and volume of solutions. The pH at the point of zero charge (pH_{pzc}) is important in order to determine the acidity/basicity and total surface charge of the GO-$MnFe_2O_4$ nanocomposites in solution and it was determined using pH drift method [32]. The pH_{pzc} of the GO-$MnFe_2O_4$ is the point where the final pH and the initial pH cut each other and was determined 6.23 as shown in Fig. S1. When the solution pH is less than the pH_{pzc}, the adsorbent surface is positively charged, and when the solution pH is greater, then the adsorbent surface becomes negatively charged which favors the adsorption of cations.

3. Results and discussion

3.1. Characterization of GO-$MnFe_2O_4$ nanocomposite

The phase purity and crystalline structure of the prepared GO-$MnFe_2O_4$ nanocomposite has shown in Fig. 1. All the diffraction patterns ensured the well-crystallized structure of spinel type $MnFe_2O_4$ phase. The diffraction peaks appeared at 2θ values of 30.52, 33.61, 36.21, 41.27, 50.13, 54.35, 62.98, 64.36 and 72.47° correspond to the (220), (311), (222), (400), (422), (511), (440), (531) and (533) crystal plan of $MnFe_2O_4$ respectively of the P-XRD pattern of GO-$MnFe_2O_4$ suggest the presence of cubic spinel structure with a fcc system which matches to the standard JCPDS file 00-010-0319 [33]. The diffraction peak appeared at 12.98° correspond to graphene oxide. The P-XRD does not show any peaks which corresponds to oxides of manganese or iron and hence indicating the purity of the synthesized sample. A careful examination of P-XRD suggest peaks shift slightly towards right hand side (higher angles) which may be due to the formation of oxygen containing groups between the sheets of GO. The chemical composition, oxidation state and bonding of the elements present in GO-$MnFe_2O_4$ nanocomposite was analyzed by XPS and is depicted in Fig. 2. The survey-scan XPS spectrum is shown in Fig. 2 (a) which exhibits compositional elements of the GO-$MnFe_2O_4$ material. The peaks observed at 284.32, 528.57, 640.12 and 710.31 eV are corresponding to the C 1s in sp^2 carbon, O 1s of adsorbed oxygen, Mn 2p, and Fe 2p species, respectively. The deficiency of any other contamination peak in the survey-scan suggests a high purity of GO-$MnFe_2O_4$ nanocomposite in the structure. The deconvoluted spectrum of the elements present in the nanocomposite is shown in Fig. 2(b–d). Fig. 2(b) depicts the core-level XPS spectrum of Mn 2p which contains two characteristic peaks situated at 640.8 eV and 652.71 eV corresponding to Mn $2p_{3/2}$ and Mn $2p_{1/2}$ states, respectively. These peaks clearly confirm the Mn^{+2} oxidation state of Mn. Fig. 2(c) shows the high-resolution XPS spectra of Fe 2p, showing two intense peaks with binding energies 709.78 eV and 723.43 eV which are corresponding to Fe $2p_{3/2}$ and Fe $2p_{1/2}$ states, respectively. The other two satellite peaks situated at binding energies of around 718.54 eV and 732.45 eV confirm the presence of Fe^{+3} only. The single peak of C 1s situated at 283.7 eV can be deconvoluted into four sub-peaks having positioned 283.74, 284.73, 285.66 and 287.91 eV indicating the existence of sp^2 with oxygen containing C-OH, C-O-C, and HO-C=O, respectively as observed in Fig. 2(d) [27]. The XPS data designate successful preparation of GO-$MnFe_2O_4$ nanocomposite [34]. The Fig. S2 (Supporting Information) shows the FT-IR spectrum which confirms the formation and functionalization of the GO-$MnFe_2O_4$ nanocomposite. The peak observed at 3434 cm^{-1} corresponding to the hydroxyl group (-OH) stretching vibration attributed to adsorbed water molecules between the layers of material [35]. The absorption peak appeared at 1395 and 837 cm^{-1} corresponding to the stretching peaks of epoxide group. The peaks at 1108 and 1590 cm^{-1} represent the alkoxy and the stretching vibrations of sp^2 hybridized carbon-carbon double bond (C=C) respectively. These observations confirm the presence of different functional groups of graphene oxide [29]. The absorption peaks appeared at 439 and 593 cm^{-1} are characteristic stretching vibrations of Mn—O and Fe—O bonds, demonstrating the presence of metal-oxygen bonds at tetrahedral and octahedral sites, respectively [35,36]. It is reported that the variations in the stretching absorption intensity and shifting of the stretching peak of Mn-Fe-O linkage in GO-$MnFe_2O_4$ nanocomposites, indicate the bonding of $MnFe_2O_4$ with GO surface via the electrostatic attraction or coordinate bond between $MnFe_2O_4$ nanoparticles and the functional groups (hydroxyl groups (–OH), acid groups (–COOH) or epoxy groups (C–O–C)) of the graphene oxide sheets [26,28].

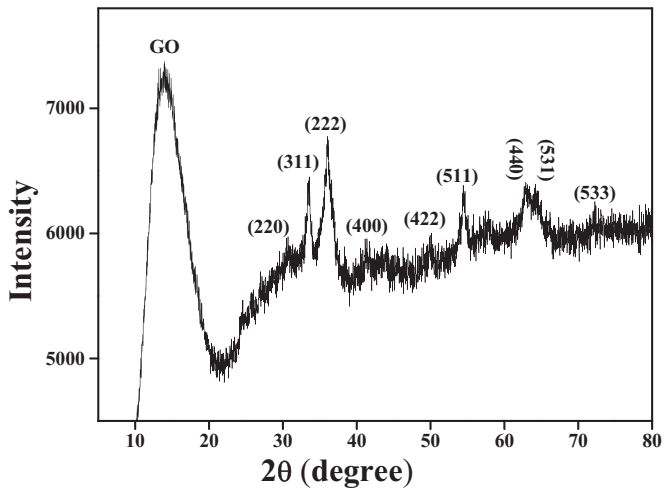

Fig. 1. XRD pattern of the synthesized GO-$MnFeO_4$nanocomposite.

Fig. 3(a) shows the surface morphology and particle size of the one-pot hydrothermally synthesized GO-$MnFe_2O_4$ nanocomposite at higher magnification. It is evident from Fig. 3 that the spherical particles of $MnFe_2O_4$ homogeneously distributed on the graphene oxide sheets. At lower magnification, particles seem aggregated on the surface of GO sheets as display in Fig. S3. Elemental mapping was performed to find out the distribution of existing species such as C, O, Mn and Fe in the prepared GO-$MnFe_2O_4$ nanocomposite and results are depicted in Fig. 3(b). The resulting elements are demonstrated in various colors such as black (C), green (O), Yellow (Mn) and blue (Fe). Also, Fig. 3 (b) shows the overlay image, confirming the uniform distribution of different elements and certifies the formation of GO-$MnFe_2O_4$ material. Fig. 3(c) shows the compositional analysis of the GO-$MnFe_2O_4$ nanocomposite, identified by EDX spectrum which confirms the weight and atomic percent of C, Mn, Fe and O. The weight percent of the GO-$MnFe_2O_4$ materials is also displayed in the form of bar and addressed in the inset of Fig. 3(c). No other foreign elements were identified in

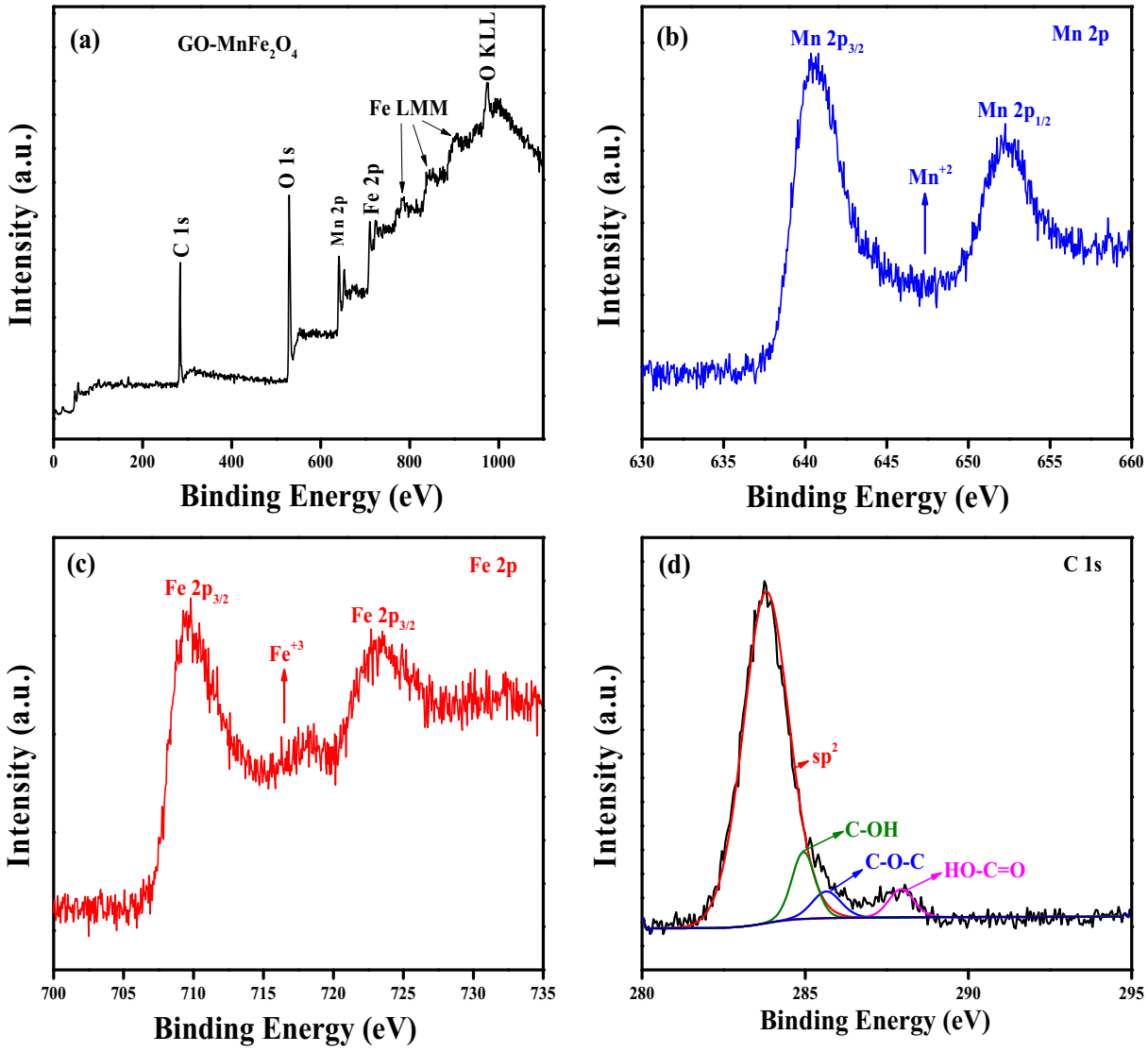

Fig. 2. XPS spectra (a) survey scan, and (b–d) deconvoluted of the synthesized GO-$MnFe_2O_4$ nanocomposite.

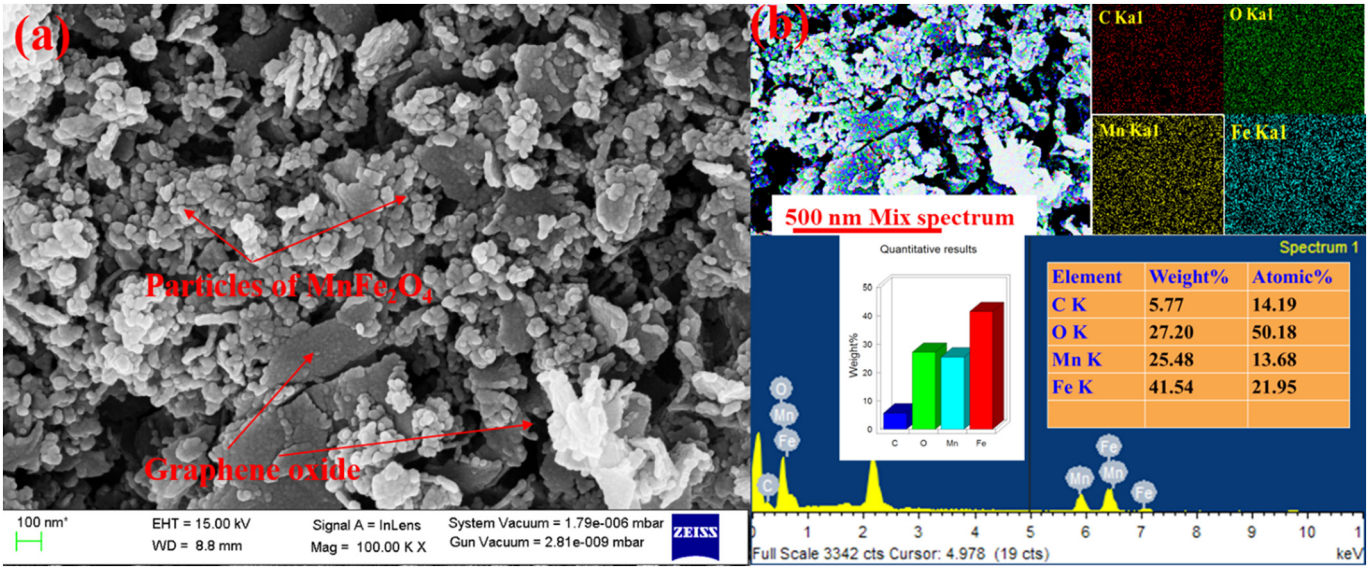

Fig. 3. (a) FE-SEM image at higher magnification and, (b) EDX image and elemental mapping of GO-$MnFe_2O_4$ nanocomposite.

the EDX analysis, confirming the formation of higher purity of GO-$MnFe_2O_4$ nanocomposite.

The nitrogen adsorption-desorption isotherm and distribution of pore size of GO-$MnFe_2O_4$ nanocomposite has been displayed in Fig. S4. The sample shows type IV isotherm curve and H3 hysteresis loop which is in accordance to International Union of Pure and Applied Chemistry (IUPAC) classification. Mesoporous nature of the solids has been confirmed due to such behavior and is related to the capillary condensation that generally occurs in the mesopore [37,38]. The BET surface area and BJH desorption pore volume were found to be 171 m^2/g and 0.423 cm^3/g, respectively. Additionally, the average pore diameter 4.12 nm has been observed for GO-$MnFe_2O_4$ nanocomposite.

3.2. pH effect

The solution pH is first important parameter to evaluate the adsorption capacity. The degree of surface charge ionization as well as speciation of the metal ions is governed by pH [33]. The adsorptive removal of Pb^{2+} ions over the GO-$MnFe_2O_4$ nanocomposite surface as a function of pH is given Fig. 4(a). In this parameter the initial concentration of Pb^{2+} ions was 50 mg/L. The adsorption capacity of the nanocomposites for Pb^{2+} ion was pH dependent and increased sharply as the pH of the solution increased from 2 to 6. The percentage removal efficiency was continuously increase from 24.89–74.06% whereas the adsorption capacity was 155.61–462.88 mg/g in the increasing range of solution pH. From these results, the conclusion is that the in strong acidic medium the adsorption efficiency was lowest. This is attributed to the fact that in strong acidic medium the H_3O^+ and metal ions are available for the existing adsorption sites and H_3O^+ has higher absorption tendency resulting in the lower adsorption capacity of metal ions [32]. As the solution pH is raised, -OH groups and -COOH groups on GO-$MnFe_2O_4$ nanocomposite are ionized to —O^- and -COO^-, respectively, which can help to improve adsorption efficiency [30]. These free H^+ ions slightly decrease the pH of the solution, as listed in Table S1 (Supporting information). Also, Pb^{2+} starts to precipitate as oxide and hydroxide at pH > 6, thus the adsorption decreases significantly. Therefore, pH 6 was selected as the optimum and used for the further experiment.

3.3. Adsorbent dose effect

Similar to pH parameter, the second important parameter is adsorbent dose for the removal efficiency of metal ion adsorption. Fig. 4 (b) displays the data of adsorption efficiency and adsorption capacity with as a function of dose concentration. It was found that the removal efficiency (%) was increased from 38.36% to 98.68% with increasing adsorbent dose from 2 to 8 mg in a 50 mL solution of Pb^{2+} ions and after that no notably change occurs in the removal efficiency even after increasing the dose up to 30 mg per 50 mL solution. This is due to availability of high surface area and a large number of vacant adsorption sites on nanocomposite with increasing adsorbent amount which makes easier penetration of Pb^{2+} to the adsorption sites. Once the equilibrium state of absorption has been achieved, the absorption dose does not have a significant effect on the dose of absorption [39]. Also, decrement in the adsorption capacity of nanocomposite occurs from 959.05

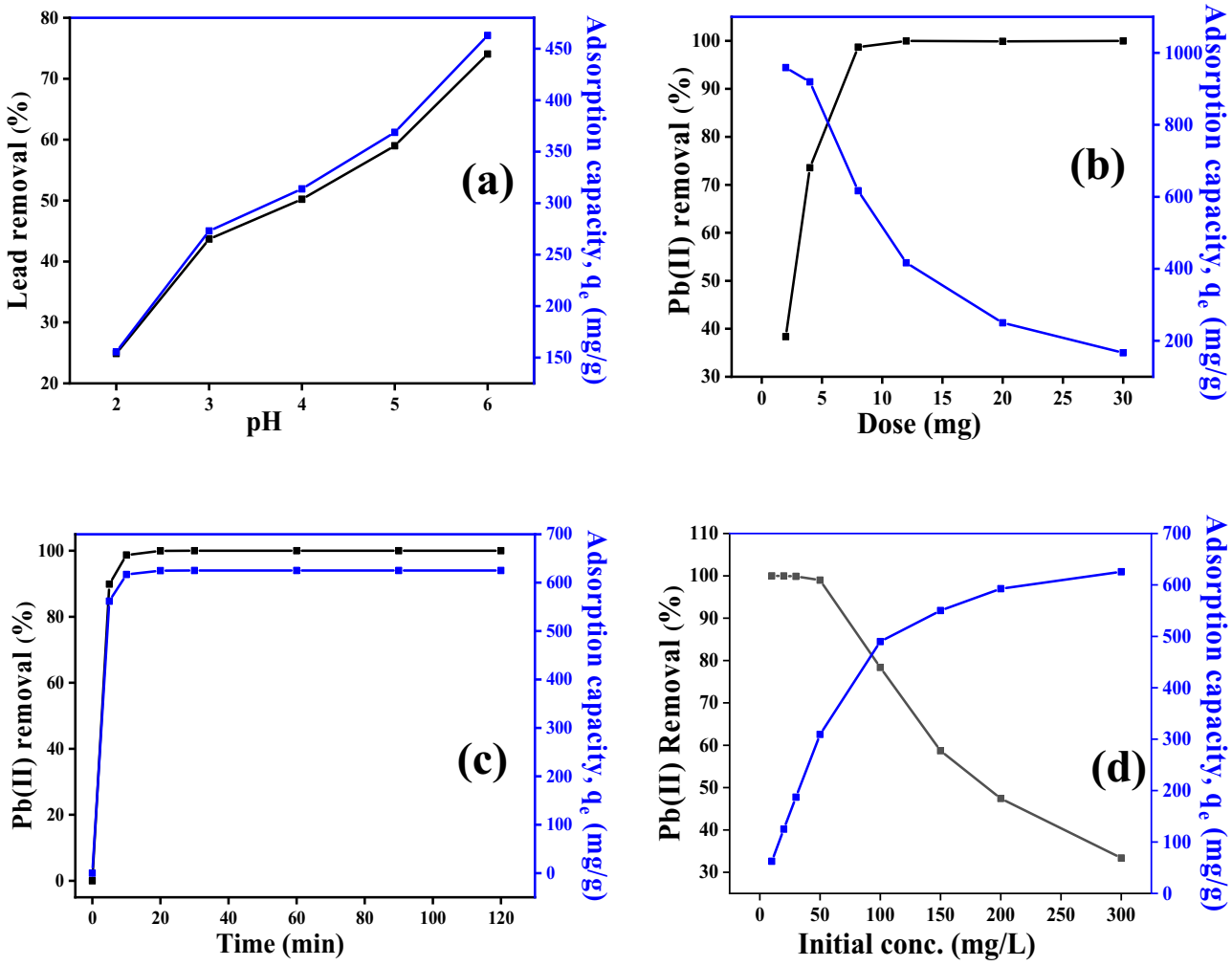

Fig. 4. Effect of (a) pH, (b) adsorbent dose, (c) contact time, and (d) initial concentration on the removal efficiency and adsorption capacity of GO-$MnFe_2O_4$ nanocomposite for Pb^{2+} ions.

to 165.63 mg/g with an increasing in dose concentration. This is attributed to the metal ions adsorption capacity to the adsorbent binding sites ratio. At high dose, the binding sites will be higher and will not saturated by the available Pb^{2+} ions which results the lesser Pb^{+2} ions adsorption on per unit mass of nanocomposite, resulting into lower adsorption capacity of nanocomposite.

3.4. Contact time effect

The adsorption rate is another important characteristic to describe the adsorption efficiency. In most of the cases, the evaluation of adsorption rate is identified by determining the equilibrium time for metal ions interaction with adsorbate. However, different adsorbents show their own equilibrium times due to different physical and chemical properties such as surface area/volume ratio, pore size and surface charge of material based on the adsorption mechanism. The adsorption efficiency and adsorption capacity for Pb^{2+} ions versus contact time has been plotted to gain inside the dependency of absorption process with time by taking a concentration 50 mg/L of Pb^{+2} ions (Fig. 4(c)). From the data, it was observed that the GO-$MnFe_2O_4$ nanocomposite adsorb the Pb^{2+} very faster and 98% absorption took place in the starting 10 min. The process then slowed down and become static in 30 min. This can be explained in the term of strong electrostatic interaction which resulted in fast dispersion of metal ions onto the surface and resulting into the covering of adsorbent surface. Data indicates that the metal ions concentration does not play a significant role on adsorption equilibrium. Hence, in each set of adsorption experiments the contact time was fixed for 120 min. so that the equilibrium could be achieved.

3.5. Pb^{2+} ions concentration effect

The concentration of metal ion had significant effect on the adsorption capacity and hence the adsorption capacity of Pb^{+2} ions with different concentrations was examined, and given in in Fig. 4(d). The data indicates that the removal efficiency of Pb^{2+} ions continuously decreased from 99.99 to 33.36% as the function of concentration. However, the adsorption capacity was increased from 62.49 to 624.51 mg/g with increase in the equilibrium concentration of Pb^{2+} ions in the solution. High removal efficiency was occurred at the lower concentration of Pb^{2+} ions which attributed to the higher surface area and number of available active sites for the adsorption. The adsorption capacity of Pb^{2+} ions was significantly lower (200 mg/L) at higher metal ions concentration. This is due to absence of effective sites for adsorption at GO-$MnFe_2O_4$ nanocomposite which limits the adsorption capacity [40].

3.6. Adsorption kinetics

Chemical reaction, particle diffusion and mass transfer mechanisms have been considered in order to understand adsorption phenomenon [41]. Kinetic models and kinetics of adsorption were studied in order to simulate the experimental data [42,43]. The rate equation of pseudo-first-order kinetics has been frequently used for the sorption in liquid/solid system and given as:

$$\ln\left(q_e - q_{t)} = \ln\ q_e - k_1 t \right. \tag{3}$$

Pseudo-second-order kinetics which are appeared to be the surface chemical reaction could be the rate determining step and specified as

$$\frac{t}{q_t} = \frac{1}{k_2 q_e^2} + \frac{t}{q_e} \tag{4}$$

where, q_t and q_e are the adsorbed amount of the Pb^{2+} (mg/g) at time t (min) and when equilibrium is achieved, respectively. The k_1 and k_2 are rate constants in min^{-1} and g/mg·min units for the pseudo-first and pseudo-second order reactions, respectively. The initial rate of adsorption can be found using following equation $h = k_2\, q_e^2$.

Fig. 5 displayed both types of kinetics models and the values of relevant parameters for linear fitting are provided in Table 1. The value of correlation coefficient (R^2) was found to be better for the pseudo-second-order model of adsorption experiments than first-order kinetic model. The better fitting in the first model specifies that the rate of adsorption for the Pb^{2+} ions on the GO-$MnFe_2O_4$ nanocomposite is being occurred by the adsorption chemistry.

In addition to this, to identified the effect of diffusion on adsorption rate, intra-particle diffusion model [44] was used as shown below

$$q_t = k_p\left(t^{1/2}\right) + C_i \tag{5}$$

The k_p (mg/g $min^{1/2}$) represent the rate constant for intra-particle diffusion and C_i is the stage intercept i (mg/g), represent the boundary layer thickness. Fig. 5(c) displays the multi-linearity when plot the data between adsorption capacity and square root of the time which shows two-phase diffusion during the adsorption phenomenon. The first phase occurs due to spreading of the adsorbate from the liquor to the adsorbent surface, indicating the faster adsorption for the GO-$MnFe_2O_4$ nanocomposite with the higher diffusion [45,46]. The second phase was the adsorbate molecules spread through the adsorbent micropores and in regions, where active sites were difficult to reach by the metals due to the cross-linking between the surface groups.

The value of intra-particle diffusion model parameters (k_p an C_i) are identified from the slope and intercept of q_t versus $t^{1/2}$, respectively for the two linear fits and listed in Table 1. Data shows that for the first linear fit, the intra-particle diffusion rate constant (kd_1) value was greater than the intra-particle diffusion rate constant (kd_2) of the second linear fit. Additionally, the value of C_1 for the first liner fit was smaller than the C_2 of the second linear fit which indicates that the adsorption rate of the Pb^{2+} ion was relatively large in the first phase and as the adsorption proceeded in the second phase the adsorption was limited due to internal diffusion. Therefore, transfer of external mass and intra-particle spread decide the overall process of adsorption. Also, intra-particle diffusion plays a crucial role in controlling the absorption process.

3.7. Adsorption isotherm

Adsorption isotherm describes the interactive behavior between the adsorption sites and adsorbate in the solution at equilibrium conditions. Several equilibrium models are available but their suitable and efficient applications are still far away from routine purpose. Therefore, it is necessary to search an equilibrium model that fitted well with the experimental data. Thus, in the current work, we employed two famous isotherm models to study the adsorption isotherms, and these are Langmuir model and Freundlich model. The Langmuir isotherm assumes that the available adsorption sites are identical and energetically equal, and only monolayer adsorption occurs in the process [47]. Langmuir equation [48] is defined according to Eq. (6) and it can be linearized as Eq. (7):

$$q_e = \frac{q_m K_L C_e}{1 + K_L C_e} \tag{6}$$

$$\frac{C_e}{q_e} = \frac{1}{K_L q_m} + \frac{C_e}{q_m} \tag{7}$$

where q_e is the equilibrium adsorption capacity (mg/g), q_m is the maximum Langmuir adsorption capability (mg/g), C_e is the equilibrium concentration (mg/L), and K_L is the Langmuir adsorption constant (L/mg). The value of K_L and q_m can be determined by intercept and slope from the linear fitting of C_e/q_e versus C_e.

Freundlich isotherm is an empirical equation which is commonly used for the heterogeneous surface on which adsorption occurs without

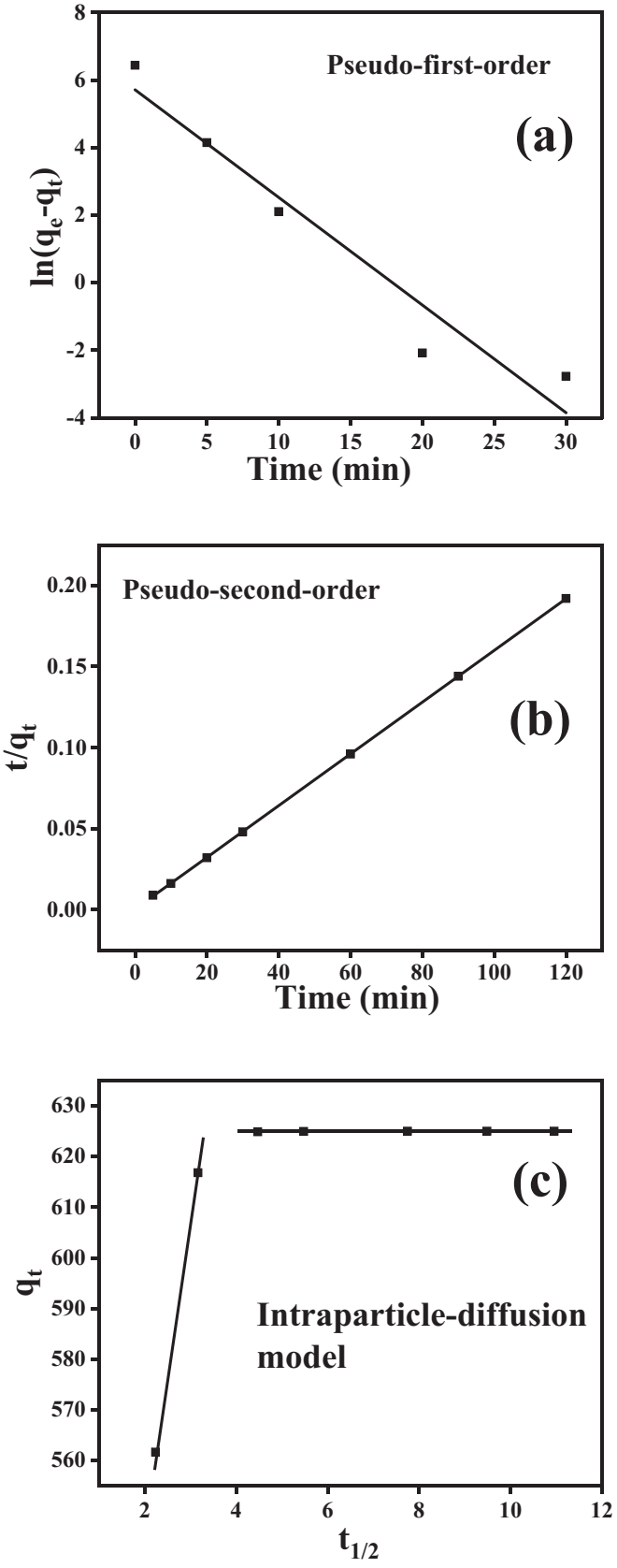

Fig. 5. Adsorption kinetics of Pb^{2+} on GO-$MnFe_2O_4$ nanocomposite at $C_o = 50$ mg/L, V/m = 6.25, pH = 3 (a) Pseudo-first-order (b) Pseudo-second-order, and (c) intra-particle diffusion model.

Table 1
Pseudo-first-order, pseudo-second-order and Intra-particle diffusion parameters for the adsorption of Pb^{2+} on the GO-$MnFe_2O_4$ nanocomposite.

Pseudo-first-order models	q_e (mg/g)	302	
	k_1 (min^{-1})	0.0318	
	R^2	0.917	
Pseudo-second-order models	q_e (mg/g)	515	
	k_2 (min^{-1})	0.0710	
	R^2	0.999	
Intra-particle diffusion model		Phase I	Phase II
	k_p (mg/g $min^{1/2}$)	524	0.0481
	C_i	128	59.5

a saturation of adsorption sites [49]. General Freundlich equation [50] is expressed in Eq. (8) and in linearized form it can be written according to Eq. (9):

$$q_e = K_F C_e^{1/n} \tag{8}$$

$$\ln q_e = \ln K_F + \frac{1}{n} \ln C_e \tag{9}$$

where, K_F and n are the Freundlich constants associated with the adsorption capacity and degree of system heterogeneity, respectively. These can be calculated from the linear fit of $\ln q_e$ versus $\ln C_e$. Larger the value of n, more heterogeneous the system.

Fig. 6 shows the adsorption isotherm data and Table 2 summarize the relevant parameters of Langmuir and Freundlich model. It is demonstrated that the experimental data of Pb^{2+} ions adsorption better fitted with the model of Langmuir isotherm ($R^2 = 0.997$) than the model of Freundlich isotherm ($R^2 = 0.974$), indicating the monolayer adsorption and uniform distribution of adsorption energy over the surface of the adsorbent. The maximum adsorption capacity was found to be 621.11 mg/g from isotherm of Langmuir model. Freundlich constant (n) was greater than 1 which implies that the GO-$MnFeO_4$nanocompositewas beneficial to the adsorption of Pb^{2+} ions.

3.8. Adsorption mechanism of Pb^{2+}

Mechanistically, the Pb^{2+} adsorption to GO-$MnFe_2O_4$ nanocomposite can be attributed to the combination of physisorption and chemisorption. (i) In physisorption, van der Waals force plays a key role between the adsorbates and the porous surface of the adsorbent. The ionic radius is reported for the Pb^{2+} is 0.119 nm [51]. As mentioned above that the GO-$MnFe_2O_4$ nanocomposite is a porous material having average pore size is 4.12 nm in which Pb^{2+} can be easily penetrate. (ii) The chemisorption of Pb^{2+} on the GO-$MnFe_2O_4$ nanocomposite can be understood by the observed effect of pH on adsorption. There are many functional groups such as -COOH and -OH over the surface of GO-$MnFe_2O_4$. At the condition of low pH, the number of protons (H^+) increase in solution and -COOH and -OH groups become positively charged -OH^{2+} and -$COOH^{2+}$, respectively. These positive charge ions lead to the decreasing in adsorption ability of Pb^{2+} ions over the surface of GO-$MnFe_2O_4$ due to electrostatic repulsion. While at higher value of pH, the -COOH, and -OH groups ionized to -COO^-, and —O^-, respectively [29]. Thus the adsorption capability of Pb^{2+} on the surface of adsorbent increases and this justification is also according to the surface complex formation theory [26,52]. According to this theory, as the value of pH increases, the competition between metal ions and protons decreases and favors the adsorption of metal ions on adsorbent surface. As mentioned earlier in Section 3.2, at higher pH (>6), there will be a decrease in the adsorption, and this is due to the formation of $Pb(OH)_2$ precipitation by Pb^{2+} ions. The adsorption of Pb^{2+} ions on the GO-$MnFeO_4$ nanocomposite surface can occur through the reaction with -OH and -COOH groups of the surface of GO-$MnFeO_4$ at optimum pH condition [26]. The following adsorption reaction on the surface of GO-$MnFeO_4$ nanocomposite is given below:

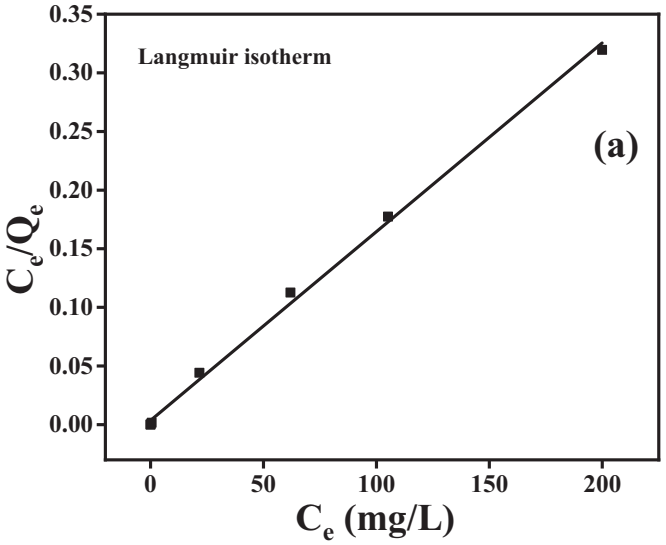

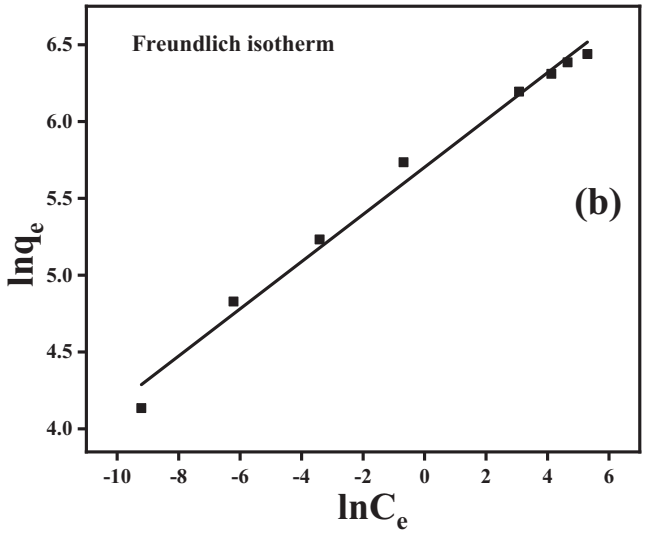

Fig. 6. Adsorption isotherm (a) Langmuir isotherm (b) Freundlich isotherm models for Pb^{2+} adsorption on GO-$MnFe_2O_4$ nanocomposite at room temperature.

Table 2
Langmuir and Freundlich isotherm parameters for the Pb^{2+} adsorption on the GO-$MnFe_2O_4$ nanocomposite.

Langmuir			Freundlich		
R^2	K_L	q_m (mg/g)	R^2	n	K_F
0.997	0.442	621.11	0.974	6.51	300

(a) Pb^{2+} react with the -OH groups of $MnFe_2O_4$ surface.

$$M\text{–}OH + Pb^{2+} \rightarrow M\text{–}O^{-}\text{–}Pb^{2+} + H^{+}$$
$$(M\text{–}OH)_2 + Pb^{2+} \rightarrow (M\text{–}O^{-})_2\text{–}Pb^{2+} + 2H^{+}$$

Here in the above adsorption reactions M is Fe and Mn [29].

(b) Pb^{2+} react with -COOH and -OH functional groups of graphene oxide surface [53].

$$GO\text{–}COOH + Pb^{2+} \rightarrow GO\text{–}COO^{-}\text{–}Pb^{2+} + H^{+}$$
$$(GO\text{–}COOH)_2 + Pb^{2+} \rightarrow (GO\text{–}COO^{-})_2\text{–}Pb^{2+} + 2H^{+}$$
$$GO\text{–}OH + Pb^{2+} \rightarrow GO\text{–}O^{-}\text{–}Pb^{2+} + H^{+}$$

3.9. Reusability

From a practical and industrial point of view, an ideal adsorbent has a good adsorption capacity and simultaneously the regeneration host material. This led to the overall less cost of the adsorbent material. Therefore, the GO-$MnFeO_4$ nanocomposite have been studied for its regeneration after the adsorption of Pb^{+2} ions from water. After the separation of GO-$MnFeO_4$ nanocomposite from solution, it was regenerated by adding 0.2 M HCl to use again in adsorption process. Fig. S5 shows the removal efficiency of Pb^{2+} up to the sixth cycles, indicating a very small change in the adsorption efficiency. This slight loss (6.0%) in the removal efficiency was attributed to the loss of few adsorption sites of the GO-$MnFe_2O_4$ nanocomposite after each adsorption-desorption process. This shows good reusability of the GO-$MnFe_2O_4$ nanocomposite as an economical material for the adsorptive removal of Pb^{2+} from wastewater.

Table 3 lists the comparison of adsorption capacity of the different adsorbent including $MnFe_2O_4$ composite synthesized using other process with the current reported one-pot hydrothermal synthesis of GO-$MnFeO_4$ nanocomposite. This comparison clearly shows that GO-$MnFeO_4$ nanocomposite has great adsorption capacity $q_m = 621.11$ mg/g as compared to other materials which indicates that sheets of graphene oxide play an effective and important role in adsorption.

4. Conclusion

The present study summarized a facile process for the preparation of GO-$MnFeO_4$ nanocomposite in one-pot using hydrothermal process. The GO-$MnFeO_4$ nanocomposite were used for the adsorptive removal of Pb^{2+} ions from water. The powder XRD, and FE-SEM analysis were used for the structural and surface morphology of synthesized nanocomposite showed a cubic spinel structure. The results of adsorption experiments suggest that the optimum adsorption for Pb^{2+} removal can be achieved at pH = 6, adsorbent dose 8 mg/50 mL for 50 mg/L The

Table 3
A comparison list of adsorption capacity of different adsorbents for Pb^{2+} ion.

Adsorbent	q_m (mg/g)	Isotherm	Kinetics	References
EDTA-GO	508	Freundlich	Pseudo-second order	[54]
Pinecone activated carbon	27.5	Langmuir	Pseudo-second order	[55]
Graphene oxide-ethylenediamine triacetic acid	455	Langmuir	–	[56]
Tetraethylenepentamine modified chitosan/$CoFe_2O_4$	228	Langmuir	Pseudo-second order	[57]
Carboxylated chitosan magnetic submicrospheres	142	Langmuir	Pseudo-second order	[58]
GO/$MnFe_2O_4$	367	Langmuir	Pseudo-second order	[29]
GO	488	Langmuir	–	[53]
$MnFe_2O_4$ nanoparticles	133	Langmuir	Pseudo-second order	[26]
TEPA-GO/$MnFe_2O_4$	263	Langmuir	Pseudo-second order	[29]
GO-$MnFe_2O_4$	621	Langmuir	Pseudo-second order	Current Work

equilibrium for adsorption was reached in 30 min, and followed to the pseudo-second-order kinetic model. This indicates that the adsorption was a chemical adsorption process. The Pb^{2+} adsorption on GO-$MnFeO_4$ nanocomposite has found to obey the Langmuir absorption isotherm indicating the monolayer adsorption. The maximum adsorption capacity for the Pb^{2+} ion on GO-$MnFeO_4$ nanocomposite has found to be 621.11 mg/g. This finding results a low-cost, stable, reusable, and promising adsorbent material for the effective removal of Pb^{+2} ions from wastewater.

CRediT authorship contribution statement

Monu Verma: Conceptualization, Writing - original draft. **Ashwani Kumar:** Data curation. **Krishna Pal Singh:** Investigation. **Ravi Kumar:** Writing - original draft. **Vinod Kumar:** Writing - original draft. **Chandra Mohan Srivastava:** Investigation. **Varun Rawat:** Investigation. **Gyandeshwar Rao:** Investigation. **Sujata Kumari:** Investigation. **Pratibha Sharma:** Investigation. **Hyunook Kim:** Writing - review & editing.

Declaration of competing interest

The authors declare that they have no known competing financial interests or personal relationships that could have appeared to influence the work reported in this paper.

Acknowledgement

The authors gratefully acknowledge to National Research Foundation of Korea (NRF) to provide the funding for research under the Korea Research Fellowship (KRF) program having grant number 2019H1D3A1A01102657. Authors are also grateful to Dr. Ramesh Chandra, Institute Instrumentation Centre (IIC), IIT Roorkee for providing FE-SEM and XPS facilities.

Appendix A. Supplementary data

Supplementary data to this article can be found online at https://doi.org/10.1016/j.molliq.2020.113769.

References

[1] S. Mohan, V. Kumar, D.K. Singh, S.H. Hasan, Effective removal of lead ions using graphene oxide-MgO nanohybrid from aqueous solution: isotherm, kinetic and thermodynamic modeling of adsorption, J. Environ. Chem. Eng. 5 (2017) 2259–2273, https://doi.org/10.1016/j.jece.2017.03.031.

[2] J. Moros, I. Llorca, M.L. Cervera, A. Pastor, S. Garrigues, M. de la Guardia, Chemometric determination of arsenic and lead in untreated powdered red paprika by diffuse reflectance near-infrared spectroscopy, Anal. Chim. Acta 613 (2008) 196–206, https://doi.org/10.1016/j.aca.2008.02.066.

[3] F. Xiao, L. Fang, W. Li, D. Wang, One-step synthesis of aluminum magnesium oxide nanocomposites for simultaneous removal of arsenic and lead ions in water, RSC Adv. 5 (2015) 8190–8193, https://doi.org/10.1039/c4ra13146k.

[4] M.E. Argun, S. Dursun, M. Karatas, M. Gürü, Activation of pine cone using Fenton oxidation for Cd(II) and Pb(II) removal, Bioresour. Technol. 99 (2008) 8691–8698, https://doi.org/10.1016/j.biortech.2008.04.014.

[5] K.C. Khulbe, T. Matsuura, Removal of heavy metals and pollutants by membrane adsorption techniques, Appl Water Sci 8 (2018) 1–30, https://doi.org/10.1007/s13201-018-0661-6.

[6] C.A. Basha, M. Somasundaram, T. Kannadasan, C.W. Lee, Heavy metals removal from copper smelting effluent using electrochemical filter press cells, Chem. Eng. J. 171 (2011) 563–571, https://doi.org/10.1016/j.cej.2011.04.031.

[7] L. Liu, J. Wu, X. Li, Y. Ling, Synthesis of poly(dimethyldiallylammonium chloride-co-acrylamide)-graft-triethylenetetramine-dithiocarbamate and its removal performance and mechanism of action towards heavy metal ions, Sep. Purif. Technol. 103 (2013) 92–100, https://doi.org/10.1016/j.seppur.2012.10.028.

[8] H.A. Aziz, M.N. Adlan, K.S. Ariffin, Heavy metals (Cd, Pb, Zn, Ni, Cu and Cr(III)) removal from water in Malaysia: post treatment by high quality limestone, Bioresour. Technol. 99 (2008) 1578–1583, https://doi.org/10.1016/j.biortech.2007.04.007.

[9] A. Lalmi, K.E. Bouhidel, B. Sahraoui, C. el H. Anfif, Removal of lead from polluted waters using ion exchange resin with $Ca(NO_3)_2$ for elution, Hydrometallurgy 178 (2018) 287–293, https://doi.org/10.1016/j.hydromet.2018.05.009.

[10] A.M. Ghaedi, M. Panahimehr, A.R.S. Nejad, S.J. Hosseini, A. Vafaei, M.M. Baneshi, Factorial experimental design for the optimization of highly selective adsorption removal of lead and copper ions using metal organic framework MOF-2 (Cd), J. Mol. Liq. 272 (2018) 15–26, https://doi.org/10.1016/j.molliq.2018.09.051.

[11] H.N. Tran, C.C. Lin, S.H. Woo, H.P. Chao, Efficient removal of copper and lead by Mg/Al layered double hydroxides intercalated with organic acid anions: adsorption kinetics, isotherms, and thermodynamics, Appl. Clay Sci. 154 (2018) 17–27, https://doi.org/10.1016/j.clay.2017.12.033.

[12] R. Huang, B. Yang, Q. Liu, Removal of chromium (VI) ions from aqueous solutions with protonated crosslinked chitosan, J. Appl. Polym. Sci. 129 (2013) 1–8, https://doi.org/10.1002/app.38685.

[13] D. Zhang, S. Wei, C. Kaila, X. Su, J. Wu, A.B. Karki, P. Young, Carbon-stabilized iron nanoparticles for environmental remediation†, Communiction 2 (2010) 917–919, https://doi.org/10.1039/c0nr00065e.

[14] Q. Shi, A. Terracciano, Y. Zhao, C. Wei, C. Christodoulatos, X. Meng, Evaluation of metal oxides and activated carbon for lead removal: kinetics, isotherms, column tests, and the role of co-existing ions, Sci. Total Environ. 648 (2019) 176–183, https://doi.org/10.1016/j.scitotenv.2018.08.013.

[15] M. Siahkamari, A. Jamali, A. Sabzevari, A. Shakeri, Removal of lead(II) ions from aqueous solutions using biocompatible polymeric nano-adsorbents: a comparative study, Carbohydr. Polym. 157 (2017) 1180–1189, https://doi.org/10.1016/j.carbpol.2016.10.085.

[16] R. Das, C.D. Vecitis, A. Schulze, B. Cao, A.F. Ismail, X. Lu, J. Chen, S. Ramakrishna, Recent advances in nanomaterials for water protection and monitoring, Chem. Soc. Rev. 46 (2017) 6946–7020, https://doi.org/10.1039/c6cs00921b.

[17] A. Ali Tahir, H. Ullah, P. Sudhagar, M. Asri Mat Teridi, A. Devadoss, S. Sundaram, The application of graphene and its derivatives to energy conversion, storage, and environmental and biosensing devices, Chem. Rec. 16 (2016) 1591–1634, https://doi.org/10.1002/tcr.201500279.

[18] G. Yu, Y. Lu, J. Guo, M. Patel, A. Bafana, X. Wang, B. Qiu, C. Jeffryes, S. Wei, Z. Guo, E.K. Wujcik, Carbon nanotubes, graphene, and their derivatives for heavy metal removal, Adv. Compos. Hybrid Mater. 1 (2018) 56–78, https://doi.org/10.1007/s42114-017-0004-3.

[19] P.C. Chiang, E.E. Chang, J.S. Wu, Comparison of chemical and thermal regeneration of aromatic compounds on exhausted activated carbon, Water Sci. Technol. 35 (1997) 279–285, https://doi.org/10.1016/S0273-1223(97)00141-8.

[20] D.H.K. Reddy, Y.S. Yun, Spinel ferrite magnetic adsorbents: alternative future materials for water purification? Coord. Chem. Rev. 315 (2016) 90–111, https://doi.org/10.1016/j.ccr.2016.01.012.

[21] N.C. Feitoza, T.D. Gonçalves, J.J. Mesquita, J.S. Menegucci, M.K.M.S. Santos, J.A. Chaker, R.B. Cunha, A.M.M. Medeiros, J.C. Rubim, M.H. Sousa, Fabrication of glycine-functionalized maghemite nanoparticles for magnetic removal of copper from wastewater, J. Hazard. Mater. 264 (2014) 153–160, https://doi.org/10.1016/j.jhazmat.2013.11.022.

[22] S.H. Hosseini, R. Rahimi, H. Kerdari, Preparation of a nanocomposite of magnetic, conducting nanoporous polyaniline and hollow manganese ferrite, Polym. J. 43 (2011) 745–750, https://doi.org/10.1038/pj.2011.47.

[23] Y. Zhu, S. Murali, W. Cai, X. Li, J.W. Suk, J.R. Potts, R.S. Ruoff, Graphene and graphene oxide: synthesis, properties, and applications, Adv. Mater. 22 (2010) 3906–3924, https://doi.org/10.1002/adma.201001068.

[24] M. Musielak, A. Gagor, B. Zawisza, E. Talik, R. Sitko, Graphene oxide/carbon nanotube membranes for highly efficient removal of metal ions from water, ACS Appl. Mater. Interfaces 11 (2019) 28582–28590, https://doi.org/10.1021/acsami.9b11214.

[25] Q.U. Ain, M.U. Farooq, M.I. Jalees, Application of magnetic graphene oxide for water purification: heavy metals removal and disinfection, J. Water Process Eng. 33 (2020), 101044. https://doi.org/10.1016/j.jwpe.2019.101044.

[26] S. Kumar, R.R. Nair, P.B. Pillai, S.N. Gupta, M.A.R. Iyengar, A.K. Sood, Graphene oxide-MnFe2O4 magnetic nanohybrids for efficient removal of lead and arsenic from water, ACS Appl. Mater. Interfaces 6 (2014) 17426–17436, https://doi.org/10.1021/am504826q.

[27] S. Chella, P. Kollu, E.V.P.R. Komarala, S. Doshi, M. Saranya, S. Felix, R. Ramachandran, P. Saravanan, V.L. Koneru, V. Venugopal, S.K. Jeong, A.N. Grace, Solvothermal synthesis of $MnFe_2O_4$-graphene composite-investigation of its adsorption and antimicrobial properties, Appl. Surf. Sci. 327 (2015) 27–36, https://doi.org/10.1016/j.apsusc.2014.11.096.

[28] X. Peng, F. Gao, J. Zhao, J. Li, J. Qu, H. Fan, Self-assembly of a graphene oxide/$MnFe_2O_4$ motor by coupling shear force with capillarity for removal of toxic heavy metals, J. Mater. Chem. A 6 (2018) 20861–20868, https://doi.org/10.1039/c8ta06663a.

[29] W. Xu, Y. Song, K. Dai, S. Sun, G. Liu, J. Yao, Novel ternary nanohybrids of tetraethylenepentamine and graphene oxide decorated with $MnFe_2O_4$ magnetic nanoparticles for the adsorption of Pb(II), J. Hazard. Mater. 358 (2018) 337–345, https://doi.org/10.1016/j.jhazmat.2018.06.071.

[30] M. Ghobadi, M. Gharabaghi, H. Abdollahi, Z. Boroumand, M. Moradian, $MnFe_2O_4$-graphene oxide magnetic nanoparticles as a high-performance adsorbent for rare earth elements: synthesis, isotherms, kinetics, thermodynamics and desorption, J. Hazard. Mater. 351 (2018) 308–316, https://doi.org/10.1016/j.jhazmat.2018.03.011.

[31] W.S. Hummers, R.E. Offeman, Preparation of graphitic oxide, J. Am. Chem. Soc. 80 (1958) 1339, https://doi.org/10.1021/ja01539a017.

[32] M. Verma, I. Tyagi, R. Chandra, V.K. Gupta, Adsorptive removal of Pb (II) ions from aqueous solution using CuO nanoparticles synthesized by sputtering method, J. Mol. Liq. 225 (2017) 936–944, https://doi.org/10.1016/j.molliq.2016.04.045.

[33] J. Chen, W. Wen, L. Kong, S. Tian, F. Ding, Y. Xiong, Magnetically separable and durable $MnFe_2O_4$ for efficient catalytic ozonation of organic pollutants, Ind. Eng. Chem. Res. 53 (2013) 6297–6306, https://doi.org/10.1021/ie403914r.

[34] Y. Fu, P. Xiong, H. Chen, X. Sun, X. Wang, High photocatalytic activity of magnetically separable manganese ferrite-Graphene heteroarchitectures, Ind. Eng. Chem. Res. 51 (2012) 725–731, https://doi.org/10.1021/ie2026212.
[35] P. Marin, R. Bergamasco, A.N. Módenes, P.R. Paraiso, S. Hamoudi, Synthesis and characterization of graphene oxide functionalized with $MnFe_2O_4$ and supported on activated carbon for glyphosate adsorption in fixed bed column, Process. Saf. Environ. Prot. 123 (2019) 59–71, https://doi.org/10.1016/j.psep.2018.12.027.
[36] Y. Zhou, B. Xiao, S.Q. Liu, Z. Meng, Z.G. Chen, C.Y. Zou, C.B. Liu, F. Chen, X. Zhou, Photo-Fenton degradation of ammonia via a manganese-iron double-active component catalyst of graphene-manganese ferrite under visible light, Chem. Eng. J. 283 (2016) 266–275, https://doi.org/10.1016/j.cej.2015.07.049.
[37] L. Robert, J. Burwell, Manual of symbols and terminology for physicochemical quantities and units-appendix II heterogeneous catalysis, Adv. Catal. 26 (1977) 351–392, https://doi.org/10.1016/S0360-0564(08)60074-7.
[38] K.C. Barick, S. Singh, M. Aslam, D. Bahadur, Porosity and photocatalytic studies of transition metal doped ZnO nanoclusters, Microporous Mesoporous Mater. 134 (2010) 195–202, https://doi.org/10.1016/j.micromeso.2010.05.026.
[39] Ö. Gerçel, H.F. Gerçel, Adsorption of lead(II) ions from aqueous solutions by activated carbon prepared from biomass plant material of Euphorbia rigida, Chem. Eng. J. 132 (2007) 289–297, https://doi.org/10.1016/j.cej.2007.01.010.
[40] W. Yin, X. Zhan, P. Fang, M. Xia, J. Yu, R.A. Chi, A facile one-pot strategy to functionalize graphene oxide with poly(amino-phosphonic acid) derived from wasted acrylic fibers for effective Gd(III) capture, ACS Sustain. Chem. Eng. 7 (2019) 19857–19869, https://doi.org/10.1021/acssuschemeng.9b05221.
[41] S. Hokkanen, E. Repo, M. Sillanpää, Removal of heavy metals from aqueous solutions by succinic anhydride modified mercerized nanocellulose, Chem. Eng. J. 223 (2013) 40–47, https://doi.org/10.1016/j.cej.2013.02.054.
[42] F. Zhao, E. Repo, M. Sillanpää, Y. Meng, D. Yin, W.Z. Tang, Green synthesis of magnetic EDTA- and/or DTPA-cross-linked chitosan adsorbents for highly efficient removal of metals, Ind. Eng. Chem. Res. 54 (2015) 1271–1281, https://doi.org/10.1021/ie503874x.
[43] Y.S. Ho, G. McKay, Pseudo-second order model for sorption processes, Process Biochem. 34 (1999) 451–465, https://doi.org/10.1021/acs.oprd.7b00090.
[44] S. Figaro, J.P. Avril, F. Brouers, A. Ouensanga, S. Gaspard, Adsorption studies of molasse's wastewaters on activated carbon: Modelling with a new fractal kinetic equation and evaluation of kinetic models, J. Hazard. Mater. 161 (2009) 649–656, https://doi.org/10.1016/j.jhazmat.2008.04.006.
[45] F. Zhao, E. Repo, D. Yin, M.E.T. Sillanpää, Adsorption of Cd(II) and Pb(II) by a novel EGTA-modified chitosan material: kinetics and isotherms, J. Colloid Interface Sci. 409 (2013) 174–182, https://doi.org/10.1016/j.jcis.2013.07.062.
[46] C. Li, Y. Yan, Q. Zhang, Z. Zhang, L. Huang, J. Zhang, Y. Xiong, S. Tan, Adsorption of Cd^{2+} and Ni^{2+} from aqueous single-metal solutions on graphene oxide-chitosan-poly(vinyl alcohol) hydrogels, Langmuir 35 (2019) 4481–4490, https://doi.org/10.1021/acs.langmuir.8b04189.
[47] Y.S. Ho, J.F. Porter, G. Mckay, Equilibrium isotherm studies for the sorption of divalent metal ionsonto peat: copper, nickel and lead single component systems, Water Air Soil Pollut. 141 (2002) 1–33, https://doi.org/10.1023/A:1021304828010.
[48] I. Langmuir, The adsorption of gases on plane surfaces of mica and platinum, J. Am. Chem. Soc. 40 (1918) 1361–1403, https://doi.org/10.1021/ja01269a066.
[49] F. Ge, M.M. Li, H. Ye, B.X. Zhao, Effective removal of heavy metal ions Cd^{2+}, Zn^{2+}, Pb^{2+}, Cu^{2+} from aqueous solution by polymer-modified mag netic nanoparticles, J. Hazard. Mater. 211–212 (2012) 366–372, https://doi.org/10.1016/j.jhazmat.2011.12.013.
[50] U. Freundlich, Die adsorption in lusungen, 1906 385–470.
[51] S. Mishra, A. Yadav, N. Verma, Carbon gel-supported Fe-graphene disks: synthesis, adsorption of aqueous Cr(VI) and Pb(II) and the removal mechanism, Chem. Eng. J. 326 (2017) 987–999, https://doi.org/10.1016/j.cej.2017.06.022.
[52] S.A. Kosa, G. Al-Zhrani, M. Abdel Salam, Removal of heavy metals from aqueous solutions by multi-walled carbon nanotubes modified with 8-hydroxyquinoline, Chem. Eng. J. 181–182 (2012) 159–168, https://doi.org/10.1016/j.cej.2011.11.044.
[53] C.J. Madadrang, H.Y. Kim, G. Gao, N. Wang, J. Zhu, H. Feng, M. Gorring, M.L. Kasner, S. Hou, Adsorption behavior of EDTA-graphene oxide for Pb(II) removal, ACS Appl. Mater. Interfaces 4 (2012) 1186–1193, https://doi.org/10.1021/am201645g.
[54] L. Cui, Y. Wang, L. Gao, L. Hu, L. Yan, Q. Wei, B. Du, EDTA functionalized magnetic graphene oxide for removal of Pb(II), Hg(II) and Cu(II) in water treatment: adsorption mechanism and separation property, Chem. Eng. J. 281 (2015) 1–10, https://doi.org/10.1016/j.cej.2015.06.043.
[55] M. Momčilović, M. Purenović, A. Bojić, A. Zarubica, M. Randelovid, Removal of lead (II) ions from aqueous solutions by adsorption onto pine cone activated carbon, Desalination 276 (2011) 53–59, https://doi.org/10.1016/j.desal.2011.03.013.
[56] I.E. Mejias Carpio, J.D. Mangadlao, H.N. Nguyen, R.C. Advincula, D.F. Rodrigues, Graphene oxide functionalized with ethylenediamine triacetic acid for heavy metal adsorption and anti-microbial applications, Carbon N. Y. 77 (2014) 289–301, https://doi.org/10.1016/j.carbon.2014.05.032.
[57] C. Fan, K. Li, J. Li, D. Ying, Y. Wang, J. Jia, Comparative and competitive adsorption of Pb(II) and Cu(II) using tetraethylenepentamine modified chitosan/$CoFe_2O_4$ particles, J. Hazard. Mater. 326 (2017) 211–220, https://doi.org/10.1016/j.jhazmat.2016.12.036.
[58] Y. Xu, Q. Dang, C. Liu, J. Yan, B. Fan, J. Cai, J. Li, Preparation and characterization of carboxyl-functionalized chitosan magnetic microspheres and submicrospheres for Pb^{2+} removal, Colloids Surfaces A Physicochem. Eng. Asp. 482 (2015) 353–364, https://doi.org/10.1016/j.colsurfa.2015.06.028.